An Improved Method for Phase Triangulation Algorithm Based on the Coherence Matrix Eigen-Decomposition in Time-Series SAR Interferometry

QIAN HE[1,2], XIN HE[3], HUIFU ZHUANG[1,2], (Member, IEEE), RUI WANG[1,2], AND JIAWEI CHEN[4]

[1]Jiangsu Key Laboratory of Resources and Environmental Information Engineering, China University of Mining and Technology, Xuzhou 221116, China
[2]School of Environment Science and Spatial Informatics, China University of Mining and Technology, Xuzhou 221116, China
[3]Hubei YJT Technology Company Ltd., Wuhan 430073, China
[4]Ganzhou Liangye Technology Company Ltd., Ganzhou 341000, China

Corresponding author: Qian He (jcchgc@163.com)

ABSTRACT Time-series SAR interferometry, which combines permanent scatterers (PSs) and distributed scatterers (DSs), has been strongly developed in recent years. Unlike PS, DS corresponds to a natural target whose neighboring pixels share similar reflectivity values. The selection of DS is relevant to the goodness-of-fit value, the estimation of which is based on all possible combined interferometric phases and fails to avoid the adverse effect of low-quality phases. This paper used eigen-decomposition of coherence matrix that was constructed based on the identified homogeneous pixels to perform phase optimization, and then only the interferometric phases with low noise and clear fringes are utilized to measure the goodness-of-fit. 30 Sentinel-1A images were applied to test the improved method of land subsidence monitoring in Beijing, China. The deformation results of different methods were cross verified and the area statistics of the study area were carried out. The results show that the maximum subsidence monitored by the improved method is located in Jinzhan Town with a maximum rate of −109 mm/yr. This improved method extracts more measurement points with accuracy ensured, which is proved to be an effective way to provide the high spatial density of deformation measurements. The land subsidence in this area is mainly caused by the excessive exploitation of groundwater resources. This research provides support for the prevention and control work of relevant departments.

INDEX TERMS Distributed scatterers (DSs), interferometric synthetic aperture radar (InSAR), land subsidence.

I. INTRODUCTION

Land subsidence is a common geological disaster with the characteristics of slow formation and wide impact [1], [2]. Permanent scatterer (PS) interferometry and small baseline subset (SBAS) interferometry are time-series InSAR techniques that has a wide application in land subsidence monitoring [3]–[18]. Furthermore, Zhang *et al.* [19]–[22] combined the advantages of PS and SBAS InSAR, and presented a new method named Multiple-master Coherent Target Small-Baseline InSAR (MCTSB-InSAR), which is a useful tool for

The associate editor coordinating the review of this manuscript and approving it for publication was Cheng Hu.

measuring ground displacement. MCTSB-InSAR uses multiple thresholds such as amplitude dispersion index, average amplitude and coherence coefficient to extract high coherent targets and local Delaunay triangulation to increase the redundancy of network connection. However, it is difficult for these methods to obtain enough measurement points (MPs) on natural land covers.

Since the SqueeSAR algorithm was put forward by Ferretti *et al.* [23], time-series InSAR technique based on distributed scatterer (DS) has gradually become a research hotspot in the field of deformation monitoring. Unlike pointwise PS, DS corresponds to a natural target whose neighboring pixels share similar reflectivity values. As we all

know, DSs are easily affected by temporal and geometrical decorrelation [24]. It is necessary to carry out phase optimization. In SqueeSAR, Kolmogorov-Smirnov (KS) test is utilized to identify statistically homogeneous pixel (SHP), and phase triangulation (PT) algorithm based on maximum likelihood (ML) estimator is applied to optimize the phase [23]. The traditional PS InSAR algorithm is used to process DS and PS to estimate the displacement of each measurement point (MP). Significantly, targets with SHP number greater than the pre-set value are considered as DS candidates, and then a certain goodness-of-fit threshold is utilized to select reliable DS from them [25]. The key of DS research lies in SHP identification and phase optimization.

Many scholars have done a series of related research on the extraction of SHP [26]–[29]. Parizzi *et al.* [30] compared and analyzed the Kullback-Leibler divergence, the KS test, the Anderson-Darling (AD) test and generalized likelihood ratio test (GLRT). Their study showed that the parametric GLRT performed best under the assumption that the amplitude satisfies the Rayleigh distribution. AD test is a special form of Cramer-von Mises (CM) test. Jiang *et al.* [31] demonstrated that Baumgartner-Weiβ-Schindler (BWS) test had higher power than KS test and CM test. However, the calculation of these tests is very time-consuming. A Fast Statistically Homogeneous Pixel Selection (FaSHPS) algorithm was presented [32], [33], which used confidence interval estimation to replace significant difference judgment of hypothesis test for the case of Rayleigh-distributed amplitudes. To further decrease the heterogeneity of SHP, Jiang *et al.* [34] improved the FaSHPS and proposed the hypothesis test of confidence interval (HTCI) algorithm, which had a higher estimation accuracy in medium and large samples [35].

After identifying the SHP, the covariance matrix can be constructed, and then the phase-estimation procedure can be carried out. Cao *et al.* [36] put forward two modified PT algorithms (equal-weighted PT and coherence-weighted PT) and analyzed the differences between published PT algorithms. To reduce the computational complexity, a method named the Component extrAction and sElection SAR (CAESAR) was presented [37], which estimated the principal phase component for DS by eigenvalue decomposition (EVD) of the covariance matrix [38]. The deformation estimation performed through the CAESAR module in MCTSB-InSAR processing chain, is hereafter defined as CAESAR-InSAR in our work. For medium or large stack sizes, it has significant advantages in computational efficiency. However, working on covariance matrix is easily affected by the unbalances of backscattered power between SAR images. These algorithms use all possible $N(N-1)/2$ interferometric phases to calculate the goodness-of-fit when evaluating the quality of phase optimization and selecting DS pixels (N is the number of SAR images), which ignores the adverse effects of low-quality interferometric phases.

In view of this, we propose an improved method for PT algorithm based on the EVD of coherence matrix. To be specific, the coherence matrix constructed by the SHPs identified

the HTCI algorithm is applied for EVD to optimize the phase. Most notably, only the interferometric phases with low noise and clear fringes are utilized to calculate the goodness-of-fit value in DS selection, which is a unique feature of the improved method. In addition, the final deformation is the result of joint processing the selected DS and PS. The improved strategy is performed in the framework of MCTSB-InSAR to extend the analysis of coherent targets interferometry and increase spatial density of deformation measurements.

In this paper, the improved method is tested for land subsidence monitoring over Beijing in China using 30 Sentinel-1A images. Besides, the monitoring results derived from different methods (MCTSB-InSAR, CAESAR-InSAR and the improved method) are compared, verified and analyzed. The rest of this paper is organized as follows: Section 2 describes the study area and datasets. Section 3 presents the methods adopted in this study. Section 4 shows the results of the experiments. Section 5 is a discussion of the obtained results. Finally, Section 6 draws the main conclusions from this work.

II. STUDY AREA AND DATASETS
A. STUDY AREA
The study area is located in the northeast of Beijing, China with geographic coordinates of 116°29′ E-116°40′ E, 39°57′ N-40°8′ N, as shown in Figure 1. The climate is hot and rainy in summer, and cold and dry in winter. The transportation is very convenient. The land cover classification of study area mainly includes water bodies (like Wenyu River), vegetation (like golf courses and parks), bare land, buildings and structures (like Beijing Capital International Airport Terminal and Airport Expressway).
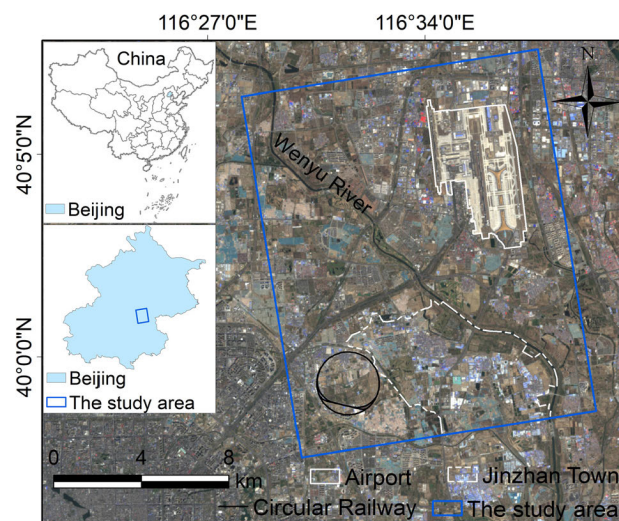

FIGURE 1. Location of the study area. The blue rectangle represents the outline of SAR images.

B. DATASETS
30 Sentinel-1A single look complex (SLC) images were acquired between 4 November 2017 and 11 November 2018

in ascending orbit. The satellite is a C-band SAR satellite with a 12-day return period. The detailed parameters of SAR data are shown in Table 1. Additionally, 30 m resolution Digital Elevation Model (DEM) collected by Advanced Land Observing Satellite (ALOS) was applied for the removal of the topographic phase.

TABLE 1. Details of the processed SAR data.

Items	Description
Satellite	Sentinel-1A
Acquisition mode	TOPS
Orbit direction	Ascending
Polarization	VV
Wavelength (cm)	5.55
Azimuth resolution (m)	13.90
Range resolution (m)	2.33
Incidence angle (deg)	43.77
Number of images	30
Time spans	4 November 2017 - 11 November 2018

III. METHODOLOGY

Time-series SAR images with size N are fine registered. After multi-looks, 1200×1000 pixels are cropped. Interferometric pairs with free combination are generated according to the pre-set thresholds of temporal and perpendicular baseline, and then M interferograms with lower noise and clearer fringes are selected. After removing the flat Earth phase and topographic phase through satellite orbit parameters and external DEM, M differential interferograms are generated. Reliable PS pixels are extracted by the threshold of amplitude dispersion index and average amplitude [19]–[22]. This section addresses DS selection and phase optimization.

A. SHP IDENTIFICATION

The HTCI algorithm is a parametric test method [34], [35], which identifies SHP by comparing the similarity between the central pixel p and the neighboring pixel q in the search window. It assumes that the single-look complex (SLC) SAR image obeys the complex circular Gaussian (CCG) distribution, and amplitude satisfies the Rayleigh distribution. For SAR image, its intensity is equal to the square of its amplitude, and the intensity I follows the exponential distribution. The probability density function (PDF) of I is defined as

$$f(I) = \frac{1}{\sigma^2} e^{-\frac{I}{\sigma^2}} \qquad (1)$$

where σ^2 is the standard deviation of exponential distribution. The comparison of the two exponential distributions I_p and I_q is equivalent to the following hypothesis testing problem. The null hypothesis H_0 and alternative hypothesis H_1 can be expressed as

$$H_0: \sigma_p^2 = \sigma_q^2 = \sigma^2 \quad H_1: \sigma_p^2 \neq \sigma_q^2 \qquad (2)$$

Suppose that $\{I_{1,p}, I_{2,p}, \cdots, I_{N,p}\}$ and $\{I_{1,q}, I_{2,q}, \cdots, I_{N,q}\}$ are samples of size N. According to the relationship

between exponential and chi-square distribution, the sum of N independent random variables follow chi-square distribution with $2N$ degrees of freedom $2\sum I_{i,p}/\sigma_p^2 \sim \chi_{2N}^2$ and $2\sum I_{i,q}/\sigma_q^2 \sim \chi_{2N}^2$. Further derivation is shown as follows [35]

$$\frac{\sigma_q^2 \bar{I}_p}{\sigma_p^2 \bar{I}_q} = \frac{\chi_{2N}^2/2N}{\chi_{2N}^2/2N} \sim F_{2N,2N} \Rightarrow \frac{\bar{I}_p}{\bar{I}_q} \overset{H_0}{\sim} F_{2N,2N} \qquad (3)$$

If H_0 is true, the ratio of the temporal average intensity $\bar{I}_p$ and $\bar{I}_q$ satisfies the F distribution with $(2N, 2N)$ degrees of freedom. Thus, the interval estimation can be described as

$$P\left\{ f_{\alpha/2;2N} < \frac{\bar{I}_p}{\bar{I}_q} < f_{1-\alpha/2;2N} \right\} = 1 - \alpha \qquad (4)$$

where $P\{\cdot\}$ stands for probability, $f_{\alpha/2;2N}$ is the $\alpha/2$ percentile of the F distribution. The initial window should be set relatively small (set to 7×7 in this work), and then the initial SHP set Ω_{init} is obtained using the formula (4). Subsequently, all pixels in Ω_{init} are averaged to gain an estimate of the central pixel $\hat{u}_p$.

The cumulative sum of the intensity map follows the standard Gamma distribution with scale parameter N. Therefore, a more accurate interval can be given by

$$P\left\{ g_{\alpha/2,N} \cdot \hat{u}_p/N < \hat{u} < g_{1-\alpha/2,N} \cdot \hat{u}_p/N \right\} = 1 - \alpha \qquad (5)$$

where $g_{\alpha/2,N}$ is the $\alpha/2$ percentile of the Gamma distribution. $\hat{u}$ represents the average intensity of the neighboring pixels in the search window.

The HTCI algorithm uses the unbiasedness of the likelihood ratio test (LRT) to reduce type I error when obtaining Ω_{init}, and the more accurate interval of the Gamma test to control the type II error. When the significance level α is given, the pixel q falling into the interval of formula (5) is homogeneous with the pixel p. Moreover, DS candidates are selected through SHP threshold.

B. PHASE OPTIMIZATION

After determining the SHP of pixel p, the sample covariance matrix C can be estimated by the following formula [36].

$$C = E\left[XX^H \right] \approx \frac{1}{N_p} \sum_{X \in \Omega} XX^H \qquad (6)$$

where $E[\cdot]$ denotes the expectation. $X = [x_1, x_2, \cdots, x_N]^T$ is the original complex observation of N SAR images. H stands for the transpose-conjugate operator. Ω represents the set of homogeneous pixels containing N_p adjacent pixels with similar backscattering properties.

To reduce the effect of unbalanced backscattered power among all the SAR images, we use the normalized data to construct the coherence matrix T for EVD. T is calculated as follows

$$T = E\left[YY^H \right] \approx \frac{1}{N_p} \sum_{Y \in \Omega} YY^H \qquad (7)$$

where $Y = [y_1, y_2, \cdots, y_N]^T$ is the normalized complex observation of N SAR images. It can be known that $E\left[|y_i|^2\right] = 1$. The connection between x_i and y_i is $y_i = x_i/\sqrt{E\left[|x_i|^2\right]}$. T is an $N \times N$ Hermitian matrix, which can be further expressed as

$$T = \begin{bmatrix} 1 & \gamma_{1,2}e^{j\phi_{1,2}} & \cdots & \gamma_{1,N}e^{j\phi_{1,N}} \\ \gamma_{2,1}e^{j\phi_{2,1}} & 1 & \cdots & \gamma_{2,N}e^{j\phi_{2,N}} \\ \vdots & \vdots & \ddots & \vdots \\ \gamma_{N,1}e^{j\phi_{N,1}} & \gamma_{N,2}e^{j\phi_{N,2}} & \cdots & 1 \end{bmatrix} \quad (8)$$

where $\gamma_{m,n}$ and $\phi_{m,n}$ are the coherence and interferometric phase obtained by the original mth image and nth image, respectively. j is the unit of imaginary part.

The EVD of T is a linear combination of outer products of the eigenvectors that weighted by the corresponding eigenvalues [37].

$$T = \sum_{i=1}^{N} \lambda_i v_i v_i^H \quad (9)$$

where the eigenvalues λ_i are arranged in decreasing order. $\lambda_1 \geq \lambda_2 \geq \cdots \geq \lambda_N$. v_i is the eigenvector relative to λ_i. Based on the principle of principal component analysis (PCA), the phase is estimated by extracting the phase of the eigenvector associated with the largest eigenvalue from the coherence matrix. The first principal component is the one associated with the first eigenvalue-eigenvector pair (λ_i, v_i). T is approximated with a single elementary scattering mechanism T_1 (where $T_1 = \lambda_1 v_1 v_1^H$). As a result, $\theta = [\theta_1, \theta_2, \cdots, \theta_N]^T$ is the optimal phase extracted from v_1.

The PT algorithm of the EVD-based phase estimator allows the separation of different contributions, thereby reducing the decorrelation caused by scattering interference. Moreover, it only uses the first principal component to optimize the phases, which is advantageous in terms of computational efficiency.

C. RELIABLE DS PIXELS SELECTION

The goodness-of-fit is the quality indicator for phase optimization. It is considered as the temporal coherence of DS and an important parameter for DS selection [25]. Previous studies have shown that the goodness-of-fit κ is calculated by all possible $N(N-1)/2$ interferometric phases before and after optimization [36]–[38].

As we all know, not all the interferometric phases are involved in the following process of deformation estimation due to the abandonment of some low-quality interferograms. It is inaccurate to estimate the value of goodness-of-fit in this way. One improvement is to select those interferometric pairs with low noise and clear fringes to measure the goodness-of-fit κ_{imp}. In light of this, the calculation formula of κ_{imp} can be expressed as

$$\kappa_{imp} = \frac{1}{M} Re\left(\sum_{s \in \Lambda}\sum_{t \in \Lambda} e^{j\phi_{s,t}} e^{-j(\theta_s - \theta_t)}\right) \quad (10)$$

where $Re(\cdot)$ denotes the real part of complex data. $\phi_{s,t}$ indicates the interferometric phase between the original sth image and tth image. θ_s and θ_t are the optimal phases of the sth image and tth image, respectively. Most notably, $t = s + 1$. Λ stands for the set of SAR images corresponding to M interferometric pairs that we select. The value of κ_{imp} is between 0 and 1. The larger the value of κ_{imp} is, the higher the coherence and the signal-to-noise ratio are.

DS selection is closely related to the goodness-of-fit value. κ_{imp} is estimated from M interferograms filtered by the improved strategy, which theoretically avoids the effect of low-quality interferometric phase. Pixels with κ_{imp} higher than a certain threshold are extracted from DS candidates, and the corresponding phase values of the original SAR images are substituted with their optimized values.

D. ESTIMATING DEFORMATION AT RELIABLE PIXELS

The deformation estimation of the improved method is performed in MCTSB-InSAR processing chain. All the pixels (reliable DS and PS pixels) are connected by the local Delaunay triangulation, which has advantages in the redundancy of network connection [21].

The observation equations between linear deformation rate, DEM error and residual phase of those two selected adjacent pixels are constructed. The least square algorithm is used to estimate the linear deformation rate and DEM error. Meanwhile, GACOS atmospheric correction model is applied for the generation of atmospheric phase [39]. After determining the linear deformation, the nonlinear deformation, noise phase and atmospheric phase are separated from the residual phase by temporal-spatial filtering algorithm [41]. Additionally, the phase unwrapping (PhU) consistency index threshold (set to 0.8 in this work) is used to determine the output mask of MP and generate the deformation products [38]. Specifically, the PhU consistency index ρ is given by $\rho = \left|\sum_{i=1}^{M} e^{jR_i}\right|/M$ (where R_i is the residual phase of the ith interferogram) [40].

The linear and nonlinear deformations combine to form a line-of-sight (LOS) displacement, which can be converted to vertical subsidence by using the cosine value of the incident angle. The subsidence map of SAR coordinate system is transformed into that of geographic coordinate system by geocoding. For better understanding, Figure 2 shows the flowchart of the improved method.

IV. RESULTS
A. SHP IDENTIFICATION AND PHASE OPTIMIZATION RESULTS

The experiments are carried out using 30 Sentinel-1A datasets ($N = 30$) based on the above principles and methods. Figure 3(a-b) is the average amplitude and SHP number when $\alpha = 5\%$. The value of each pixel in Figure 3(b) represents the number of SHP identified by the HTCI algorithm in a 15×15 search window. The SHP number of 0 indicates that there are no homogeneous pixels in the window, which may be due
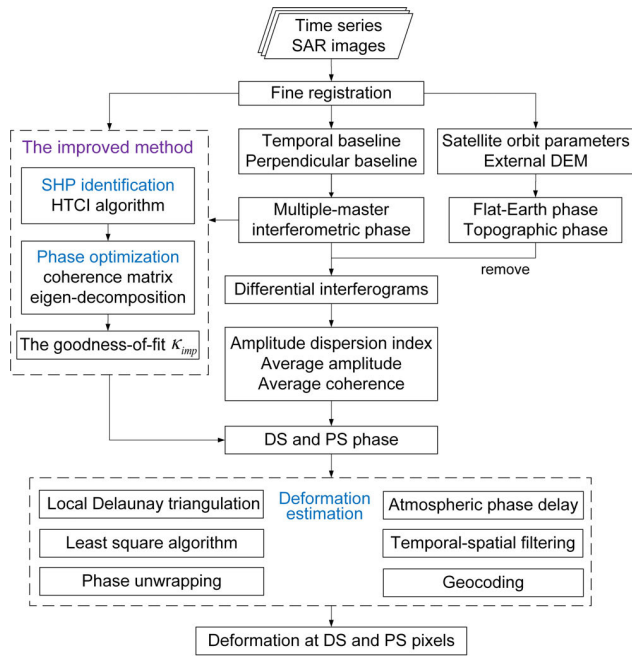
FIGURE 2. Flow chart of the improved method we proposed.

to isolated PS or noise points. The number of SHP is 224, indicating that all pixels in the window are homogeneous. It can be found that SHP number is particularly associated with the land cover type. Pixels in vegetation show large SHP number, but this is not the case in buildings and structures where the number of SHP is relatively small. Most PS targets correspond to isolated pixels with a small number of SHPs. To be specific, 90% of PS pixels with temporal coherence greater than 0.8 have less than 38 SHP, so we regard 38 as the threshold of SHP number to select DS candidates.

As is known to all, 435 interferometric pairs can be generated from the free combination of 30 images. By setting the threshold of temporal baseline (120 days) and perpendicular baseline (150 m), multiple-master interferograms can be generated. Afterwards we select 83 interferograms ($M = 83$) with less noise and clearer fringes. The distribution of interferometric pairs is shown in Figure 4. It should be noted that the spatiotemporal baseline map is composed of closed loops. The two interferograms that do not involve any loop may affect the performance of PT and phase unwrapping.

To compare the differences of phase optimization between the classical CAESAR algorithm and improved method, we calculate the goodness-of-fit values obtained by the two algorithms (see Figure 5). Furthermore, the percentage of goodness-of-fit values are shown in Figure 6. The goodness-of-fit value in vegetation is smaller than that in buildings and structures, and higher than that in water area. The average goodness-of-fit values of the two algorithms (CAESAR and the improved strategy) are 0.639 and 0.732, respectively. Obviously, 97% of pixels in Figure 5(b) show greater goodness-of-fit than that in Figure 5(a), which demonstrates that the phase quality of the improved strategy is better than that of the classical CAESAR algorithm. We consider pixels with goodness-of-fit greater than 0.8 as reliable DS pixels in this work. The percentages of pixels with goodness-of-fit greater than 0.8 in Figure 5(a-b) are 25% and 37%, respectively. It indicates that the improved strategy increases the possibility of high density of measurement points.

B. DEFORMATION RATES ANALYSIS
As mentioned in the first and three section, the improved method is implemented in MCTSB-InSAR processing chain and makes the modification based on CAESAR algorithm.
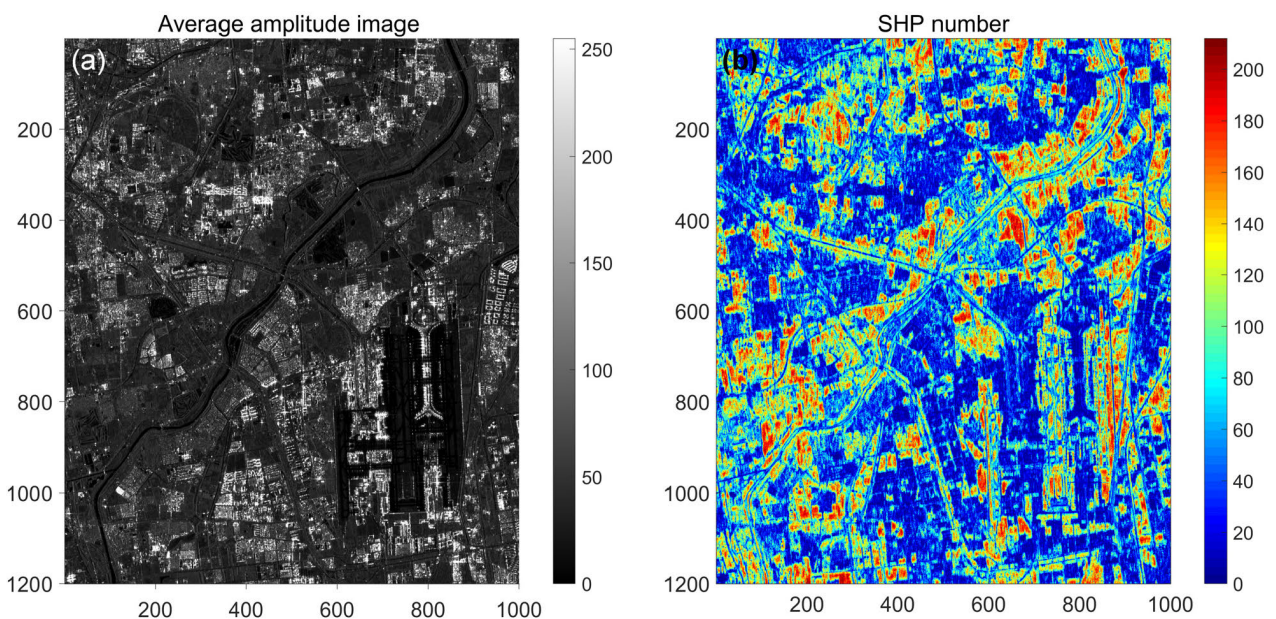

FIGURE 3. (a) The average amplitude image. (b) The map of SHP number.
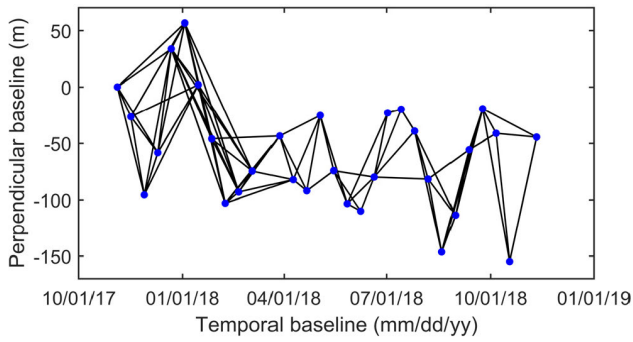
FIGURE 4. Distribution of multiple-master interferometric pairs. Blue dots indicate SAR images and black lines denote interferograms.

To testify the effectiveness of the improved method, we check the reliability of its PhU and compare its deformation monitoring results with those of the other two methods (MCTSB-InSAR, CAESAR-InSAR).

Figure 7 shows the histogram of the PhU consistency index ranging from 0 to 1. The closer its value is to 1, the smaller the residual error generated in the PhU process is. The average PhU consistency indexes of the three methods (MCTSB-InSAR, CAESAR-InSAR, and the improved method) are 0.968, 0.977 and 0.981, respectively. As can be seen from Figure 7, the right peak of the graph of the improved method moves to 1, and is characterized by a highest number of occurrences. It indicates that the PhU of the improved method outperforms the other two methods.

Figure 8 is the deformation rate of study area obtained by different methods. The location and magnitude of land subsidence in Figure 8(a-c) are roughly the same. There is no land subsidence in the northwest of the study area. Noticeable

land subsidence (≤ -10 mm/yr) is situated in the south and northeast of the study area, especially in Jinzhan Town.

Some MPs are concentrated in the area where buildings and structures (such as residential buildings, Airport Terminal and Expressway) are gathered, which are reliable PS pixels. Some MPs correspond to natural targets, which are reliable DS pixels. There is no MP in the water area (for example Wenyu River) due to the relatively low coherence.

There are 95,991 points in Figure 8(a) with the maximum rate value of -107 mm/yr, while 158,752 points are visible in Figure 8(b) with the maximum rate value of -107 mm/yr. Unlike Figure 8(a-b), Figure 8(c) shows 250,059 points with the maximum deformation rate of -109 mm/yr. It can be found that the number of MPs in Figure 8(c) is about 2.6 times that in Figure 8(a), and 1.6 times that in Figure 8(b). Compared with Figure 8(a), the additional MPs in Figure 8(b) are extracted by the CAESAR algorithm. In addition, the additional MPs in Figure 8(c) are a proof of the increase in the number of MP selected by the improved strategy.

To compare the three monitoring results in detail, we make statistics on the number of MPs and maximum deformation rate of the three representative subareas (the area occupied by the Circular Railway, Airport, and Jinzhan Town) in the study area, as shown in Figure 9. It can be found that the improved method obtains more MPs in the three subareas than the other two methods. Most of the additional MPs are located in debris areas and non-cultivated land with short vegetation. Moreover, there is little difference (no more than 4 mm/yr) between the maximum deformation rate monitored by the three methods in three subareas, which can be accepted in the experiment.

From the results, more reliable coherent targets (DS and PS) have a beneficial effect on the construction of dense
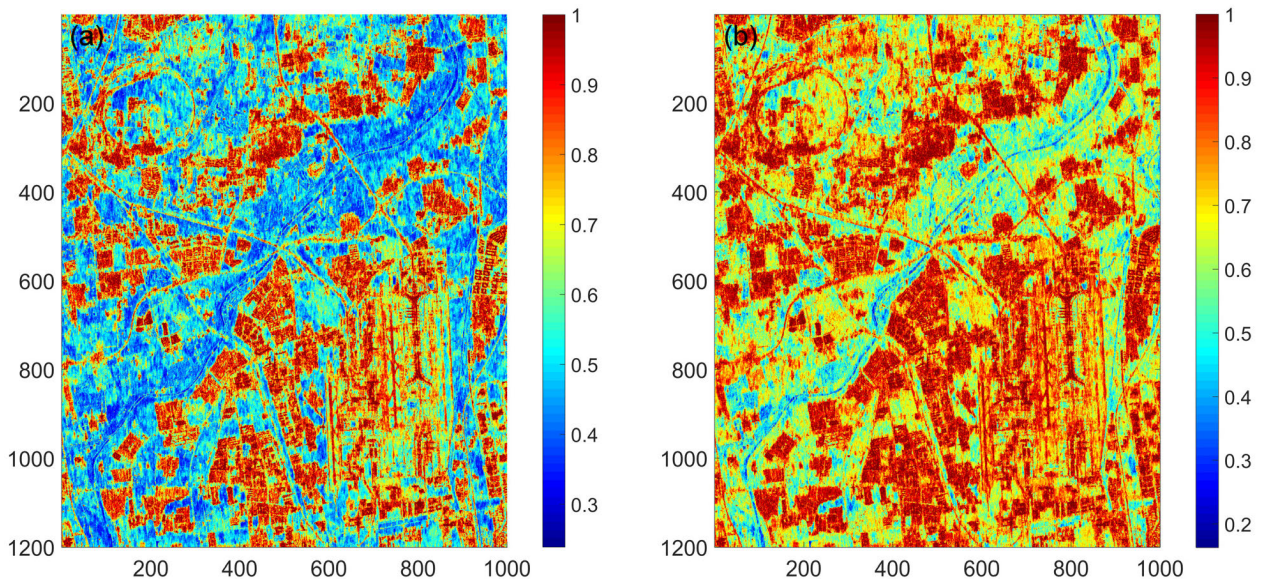

FIGURE 5. The goodness-of-fit values calculated by different methods. (a) The CAESAR algorithm (b) The improved method.
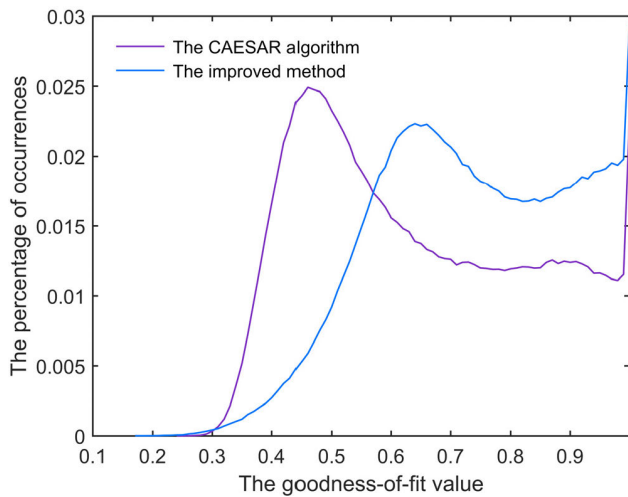
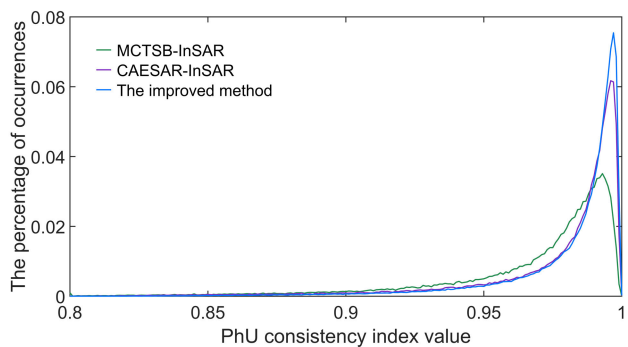**FIGURE 6.** Histograms of the goodness-of-fit values corresponding to Figure 5.

FIGURE 7. Histograms of the PhU consistency indexes estimated by three different methods.

Delaunay triangulation for PhU and better consistency of the unwrapping process. The improved method has advantages of high-density MP.

V. DISCUSSION

A. VERIFICATION OF MONITORING RESULTS

During the monitoring period, we are unable to obtain the measured leveling data. To verify the monitoring results of different methods (MCTSB-InSAR, CAESAR-InSAR, and the improved method), the linear regression analysis is carried out on the deformation rates of completely coincident points in the whole study area. The correlation coefficient r is used to measure the degree of close correlation between the two methods [29], [42], as shown in Figure 10. Assuming that υ and μ represent the deformation rates obtained by two different methods, their correlation coefficient P can be expressed as

$$P = \frac{Cov\,(\upsilon, \mu)}{\sqrt{D\,(\upsilon)}\sqrt{D\,(\mu)}} \tag{11}$$

where $Cov(\cdot)$ and $D(\cdot)$ denote the covariance and variance, respectively. The value range of P is from 0 to 1. The larger the P is, the stronger the correlation between υ and μ is.

TABLE 2. Dangerous grading and area statistics.

Evaluation factors	Grading index	Grading name	Area (km²)
Deformation rate (mm/yr)	(-30, -10]	Low dangerous	36.861
	(-50, -30]	Medium dangerous	15.851
	(-100, -50]	High dangerous	12.135
	⩽-100	Very high dangerous	0.095

The value of P is 0.973 in Figure 10(a), which demonstrates that Figure 8(b) is relatively close to Figure 8(a). The correlation coefficient P between Figure 8(a) and Figure 8(c) is 0.970, which indicates that the deformation rates in Figure 8(c) are in consistency with those in Figure 8(a). Besides, the Root Mean Square Error (RMSE) of Figure 10(a-b) is 5.885 and 5.982, respectively. This means that the monitoring results of improved method are as accurate as those of MCTSB-InSAR and CAESAR-InSAR methods. Therefore, the monitoring results of the improved method are credible. Overall, the improved method is an effective way to increase the density of deformation measurements.

B. DAMAGE CAUSED BY LAND SUBSIDENCE

To obtain the detailed damage information caused by land subsidence, dangerous assessment and area statistics are performed based on the results of the improved method. Previous studies have shown that there are different dangerous assessment indexes in different areas and actual conditions [42]–[44]. In this paper, areas with deformation rate less than −10 mm/yr are considered as dangerous areas, which are classified into four groups. According to the dangerous grading index, the area statistics of the study area are carried out (see Table 2).

The subsidence area (less than −10mm/yr) of the study area is approximately 64.942 km², accounting for about 28% of the total area. The area occupied by the Circular Railway and the northwest of the Airport belong to medium and high dangerous areas. The very high dangerous area is situated in Jinzhan Town. The damage caused by land subsidence will bring hidden dangers to people's lives and the sustainable development of society.

By analyzing the existing data [45]–[47], it can be known that the spatial distribution of the land subsidence has a high consistency with that of the groundwater level in the same period. A large amount of groundwater is exploited for residents' life, particularly in densely populated Jinzhan town. Grassland, cultivated land and woodland also need water for irrigation. The excessive exploitation of groundwater resources is the major reason of subsidence in the study area. For the Airport, the apparent differential subsidence in the northwest and southeast is mainly caused by the Shunyi ground fissure developed by the Shunyi-Liangxian fault structure. In view of this, the related department should pay special attentions to this matter and take corresponding prevention actions.
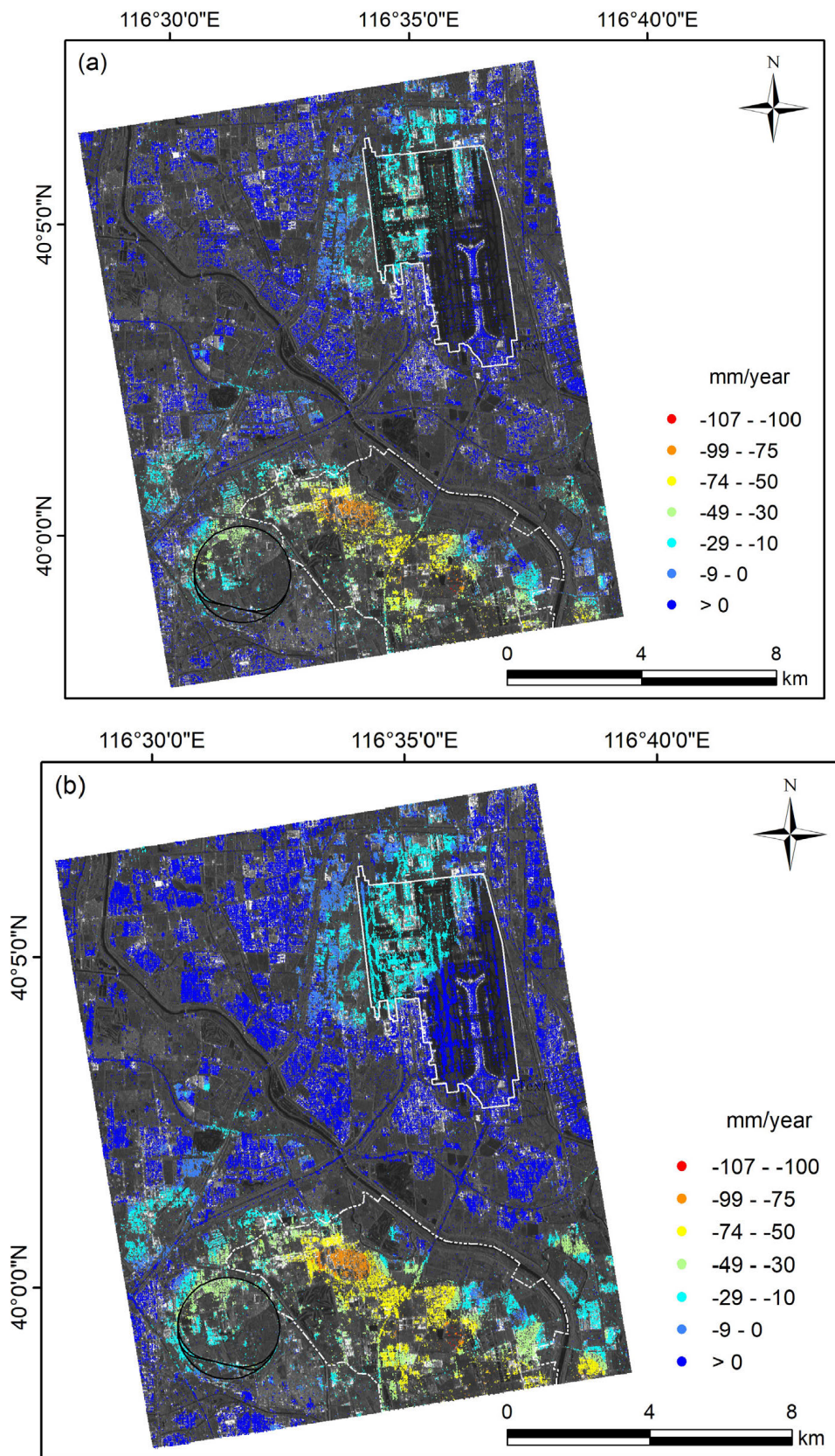
FIGURE 8. Deformation rates derived from Sentinel-1A images superimposed onto the average amplitude with different methods. (a) MCTSB-InSAR (b) CAESAR-InSAR (c) The improved method.

FIGURE 8. *(Continued.)* Deformation rates derived from Sentinel-1A images superimposed onto the average amplitude with different methods. (a) MCTSB-InSAR (b) CAESAR-InSAR (c) The improved method.
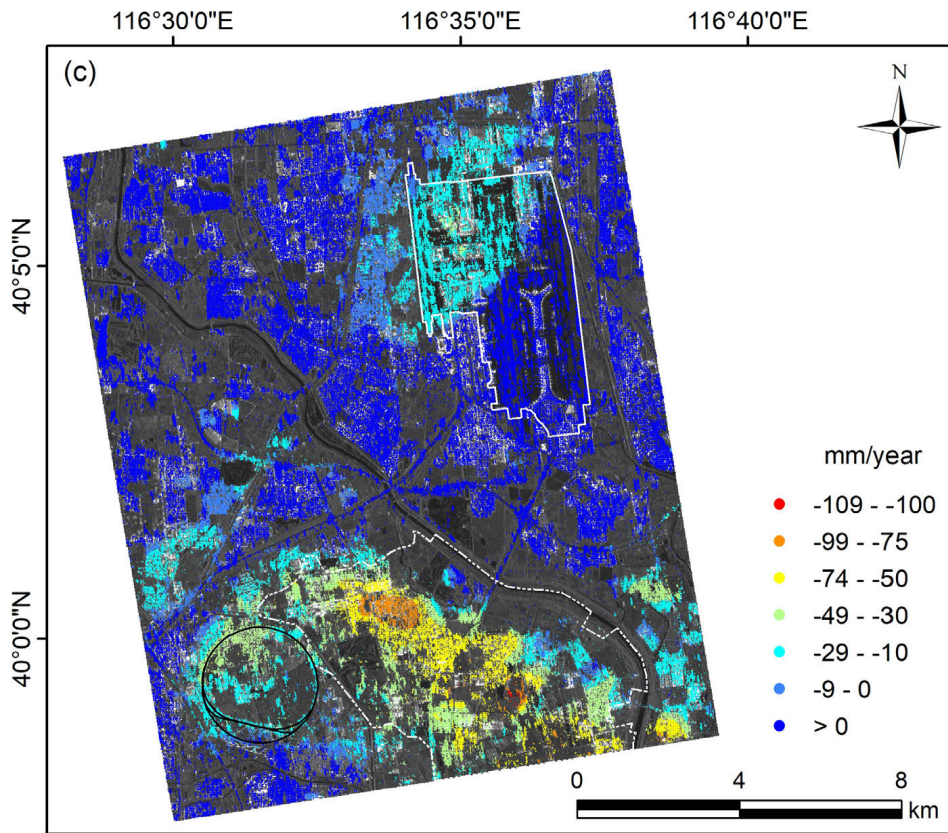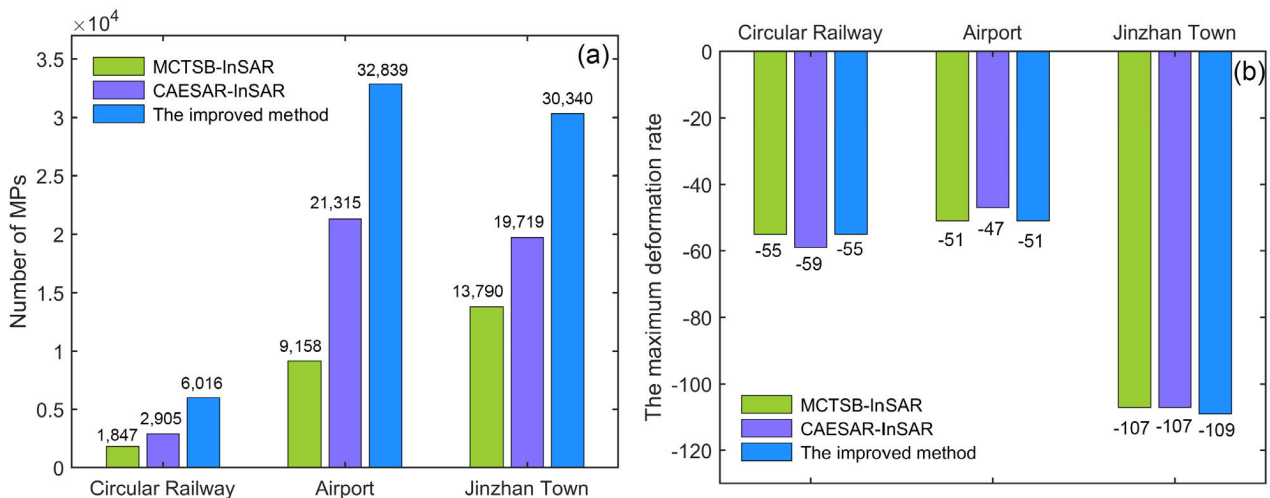

FIGURE 9. The Number of MPs and maximum deformation rate obtained by three methods in three subareas, respectively.

C. LIMITATION AND FUTURE WORK

In this work, we use the coherence matrix eigen-decomposition for DS phase optimization. The construction of coherence matrix is an important part in this process. It can be seen from formula (8) that the elements of the coherence matrix can be expressed as the product of the coherence and interferometric phase. A follow-on research direction is to further refine the coherence matrix by using

the accurately estimated coherence. The bias of the coherence can be mitigated with bootstrap, second kind statistics or other improved algorithms. Further research will follow this idea to practice.

In addition, the study area we selecte includes the largest subsidence region in Beijing and some areas with representative buildings, which has relatively high spatial coherence and is beneficial to deformation estimation. However, the
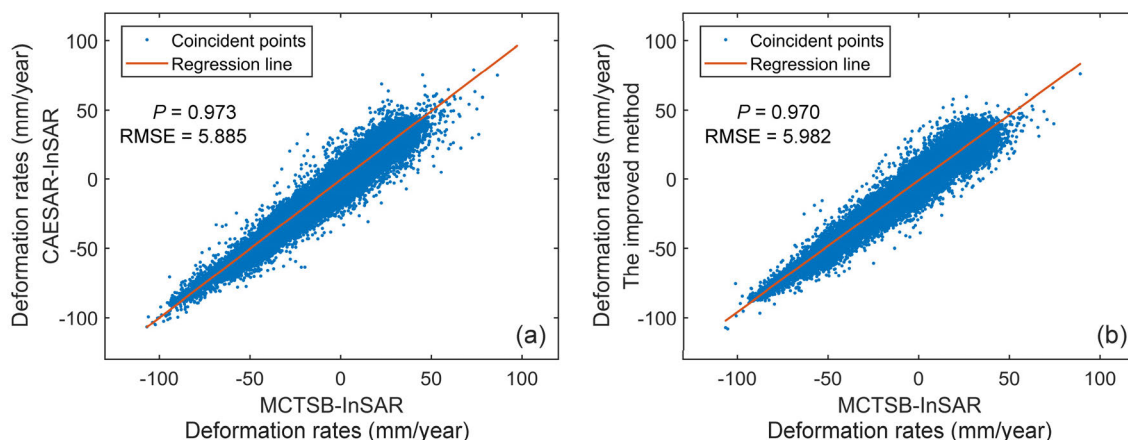
FIGURE 10. The scatter diagram and correlation of completely coincident points' deformation rates. (a) correlation between Figure 8(a-b), (b) correlation between Figure 8(a) and Figure 8(c). The horizontal and vertical axes respectively represent the deformation rates obtained by two different methods.

area proportion of buildings and structures is larger than that covered by natural targets. To highlight the advantages of the improved method, the study area will be re-selected in the future, and long time-series SAR images will be used for the real-time monitoring of land subsidence

VI. CONCLUSION

An improved method for phase triangulation algorithm based on the coherence matrix eigen-decomposition is proposed in time-series InSAR to extend the analysis of coherent targets interferometry. Specifically, SHP identified by the HTCI algorithm, and the coherence matrix is estimated according to the mean value of the pixels in SHP patch rather than that in the boxcar window. The optimized phase is obtained by EVD of coherence matrix on the basis of PCA, which has obvious advantages in computational efficiency. A unique feature of the improved method is that the goodness of fit is estimated by the interference phase of low noise and clear fringes. This strategy can accurately estimate the goodness-of-fit for evaluating the quality of phase optimization and selecting DS targets.

Our experiments are conducted using 30 Sentinel-1A images collected between 4 November 2017 and 11 November 2018 over Beijing. We compare the PhU consistency indexes estimated by three different methods (MCTSB-InSAR, CAESAR-InSAR and the improved method) and verify the monitoring results through the correlation coefficient calculated from the deformation rate of the completely coincident points obtained by different methods. Furthermore, the area statistics of the study area are implemented, and the causes of land subsidence are briefly analyzed.

The results show that the improved method performs better than the other two methods during the process of PhU, and increases the density of MPs with measurement accuracy ensured. The area most seriously affected by land subsidence is Jinzhan Town with a maximum rate of -109 mm/yr.

The main influencing factors of land subsidence is the exploitation of groundwater resources. All the information is helpful for the prevention and control work of relevant departments.

REFERENCES

[1] B. Chen, "A study on InSAR for subsidence monitoring in mining area," Ph.D. dissertation, China Univ. Mining Technol., Xuzhou, China, 2015.

[2] Y. Chen, K. Tan, S. Yan, K. Zhang, H. Zhang, X. Liu, H. Li, and Y. Sun, "Monitoring land surface displacement over Xuzhou (China) in 2015–2018 through PCA-based correction applied to SAR interferometry," *Remote Sens.*, vol. 11, p. 1494, Jun. 2019, doi: 10.3390/rs11121494.

[3] H. Fan, X. Gao, J. Yang, K. Deng, and Y. Yu, "Monitoring mining subsidence using a combination of phase-stacking and offset-tracking methods," *Remote Sens.*, vol. 7, no. 7, pp. 9166–9183, 2015, doi: 10.3390/rs70709166.

[4] Z. Yang, Z. Li, J. Zhu, A. Preusse, H. Yi, J. Hu, G. Feng, and M. Papst, "Retrieving 3-D large displacements of mining areas from a single amplitude pair of SAR using offset tracking," *Remote Sens.*, vol. 9, no. 4, p. 338, 2017, doi: 10.3390/rs9040338.

[5] X. Liu, Y. Wang, and S. Yan, "Ground deformation associated with exploitation of deep groundwater in Cangzhou city measured by multi-sensor synthetic aperture radar images," *Environ. Earth Sci.*, vol. 76, no. 1, Dec. 2016, doi: 10.1007/s12665-016-6311-0.

[6] Z. Du, L. Ge, A. H. Ng, and X. Li, "Investigation on mining subsidence over Appin–West Cliff Colliery using time-series SAR interferometry," *Int. J. Remote Sens.*, vol. 39, no. 5, pp. 1528–1547, Jan. 2018, doi: 10.1080/01431161.2017.1407501.

[7] J. Li, F. Gao, J. Lu, and T. Tao, "Deformation monitoring and prediction for residential areas in the Panji mining area based on an InSAR time series analysis and the GM-SVR model," *Open Geosci.*, vol. 11, no. 1, pp. 738–749, Nov. 2019, doi: 10.1515/geo-2019-0058.

[8] Y. Chen, Y. Tong, and K. Tan, "Coal mining deformation monitoring using SBAS-InSAR and offset tracking: A case study of yu county, China," *IEEE J. Sel. Topics Appl. Earth Observ. Remote Sens.*, vol. 13, pp. 6077–6087, 2020, doi: 10.1109/JSTARS.2020.3028083.

[9] L. Wang, K. Deng, and M. Zheng, "Research on ground deformation monitoring method in mining areas using the probability integral model fusion D-InSAR, sub-band InSAR and offset-tracking," *Int. J. Appl. Earth Observ. Geoinf.*, vol. 85, Mar. 2020, Art. no. 101981, doi: 10.1016/j.jag.2019.101981.

[10] J. Huang, Y. Bai, S. Lei, and K. Deng, "Time-series SBAS pixel offset tracking method for monitoring three-dimensional deformation in a mining area," *IEEE Access*, vol. 8, pp. 118787–118798, 2020, doi: 10.1109/ACCESS.2020.3004460.

[11] A. Ferretti, C. Prati, and F. Rocca, "Permanent scatterers in SAR interferometry," in *Proc. IEEE Int. Geosci. Remote Sens. Symp. (IGARSS)*, Jun./Jul. 1999, pp. 1528–1530, doi: 10.1109/IGARSS.1999.772008.

[12] A. Ferretti, C. Prati, and F. Rocca, "Nonlinear subsidence rate estimation using permanent scatterers in differential SAR interferometry," *IEEE Trans. Geosci. Remote Sens.*, vol. 38, no. 5, pp. 2202–2212, Sep. 2000, doi: 10.1109/36.868878.

[13] P. Berardino, G. Fornaro, R. Lanari, and E. Sansosti, "A new algorithm for surface deformation monitoring based on small baseline differential SAR interferograms," *IEEE Trans. Geosci. Remote Sens.*, vol. 40, no. 11, pp. 2375–2383, Nov. 2002, doi: 10.1109/TGRS.2002.803792.

[14] A. Hooper, "A multi-temporal InSAR method incorporating both persistent scatterer and small baseline approaches," *Geophys. Res. Lett.*, vol. 35, no. 16, Aug. 2008, Art. no. L16302, doi: 10.1029/2008GL034654.

[15] G. Liu, S. M. Buckley, X. Ding, Q. Chen, and X. Luo, "Estimating spatiotemporal ground deformation with improved persistent-scatterer radar interferometry," *IEEE Trans. Geosci. Remote Sens.*, vol. 47, no. 9, pp. 3209–3219, Sep. 2009, doi: 10.1109/TGRS.2009.2028797.

[16] Y. Liu, C. Zhao, Q. Zhang, C. Yang, and J. Zhang, "Land subsidence in Taiyuan, China, monitored by InSAR technique with multisensor SAR datasets from 1992 to 2015," *IEEE J. Sel. Topics Appl. Earth Observ. Remote Sens.*, vol. 11, no. 5, pp. 1509–1519, May 2018, doi: 10.1109/JSTARS.2018.2802702.

[17] X. Xu, D. Zhao, C. Ma, and D. Lian, "Monitoring subsidence deformation of Suzhou subway using InSAR timeseries analysis," *IEEE Access*, vol. 9, pp. 3400–3416, 2021, doi: 10.1109/ACCESS.2020.3047574.

[18] Z. Yu, G. Huang, C. Zhang, and X. Zhao, "SBAS-InSAR deformation reconstruction based on low-rank matrix completion in Southern Zibo, China," *Arabian J. Geosci.*, vol. 14, no. 4, pp. 1–9, Feb. 2021, doi: 10.1007/s12517-021-06533-5.

[19] Y. Zhang, B. Liu, H. Wu, X. Cheng, and Y. Kang, "Ground subsidence in Xiong'an New Area from 2012 to 2016 monitored by InSAR technique," *J. Earth Sci. Environ.*, vol. 40, no. 5, pp. 652–662, Sep. 2018.

[20] Y. Zhang, M. Li, H. Wu, B. Liu, Y. Kang, and Q. He, "Ground subsidence monitoring over full territory of Jiangsu province with InSAR," *Sci. Surv. Mapp.*, vol. 44, no. 6, pp. 114–120, Jun. 2019.

[21] Y. Zhang, H. Wu, Y. Kang, and C. Zhu, "Ground subsidence in the Beijing-Tianjin-Hebei region from 1992 to 2014 revealed by multiple SAR stacks," *Remote Sens.*, vol. 8, no. 8, p. 675, Aug. 2016, doi: 10.3390/rs8080675.

[22] Y. Zhang, H. Wu, M. Li, Y. Kang, and Z. Lu, "Investigating ground subsidence and the causes over the whole Jiangsu province, China using sentinel-1 SAR data," *Remote Sens.*, vol. 13, no. 2, p. 179, Jan. 2021, doi: 10.3390/rs13020179.

[23] A. Ferretti, A. Fumagalli, F. Novali, C. Prati, F. Rocca, and A. Rucci, "A new algorithm for processing interferometric data-stacks: SqueeSAR," *IEEE Trans. Geosci. Remote Sens.*, vol. 49, no. 9, pp. 3460–3470, Sep. 2011, doi: 10.1109/TGRS.2011.2124465.

[24] N. Cao, H. Lee, and H. C. Jung, "A phase-decomposition-based PSInSAR processing method," *IEEE Trans. Geosci. Remote Sens.*, vol. 54, no. 2, pp. 1074–1090, Feb. 2016, doi: 10.1109/TGRS.2015.2473818.

[25] J. Liu, Y. Wang, Y. Li, L. Dang, X. Liu, H. Zhao, and S. Yan, "Underground coal fires identification and monitoring using time-series InSAR with persistent and distributed scatterers: A case study of Miquan coal fire zone in Xinjiang, China," *IEEE Access*, vol. 7, pp. 164492–164506, 2019, doi: 10.1109/ACCESS.2019.2952363.

[26] Y. Wang, Y. Deng, W. Fei, R. Wang, H. Song, J. Wang, and N. Li, "Modified statistically homogeneous Pixels' selection with multitemporal SAR images," *IEEE Geosci. Remote Sens. Lett.*, vol. 13, no. 12, pp. 1930–1934, Dec. 2016, doi: 10.1109/LGRS.2016.2618766.

[27] H. Song, Y. Sun, R. Wang, B. Zhang, N. Li, Y. Wang, and W. Fei, "Statistically homogeneous pixel selection for small SAR data sets based on the similarity test of the covariance matrix," *Remote Sens. Lett.*, vol. 8, no. 10, pp. 927–936, Jun. 2017, doi: 10.1080/2150704X.2017.1335907.

[28] K.-F. Lin and D. Perissin, "Identification of statistically homogeneous pixels based on one-sample test," *Remote Sens.*, vol. 9, no. 1, p. 37, 2017, doi: 10.3390/rs9010037.

[29] Y. Liu, H. Fan, L. Wang, and H. Zhuang, "Monitoring of surface deformation in a low coherence area using distributed scatterers InSAR: Case study in the xiaolangdi basin of the Yellow river, China," *Bull. Eng. Geol. Environ.*, vol. 80, no. 1, pp. 25–39, Jan. 2021, doi: 10.1007/s10064-020-01929-1.

[30] A. Parizzi and R. Brcic, "Adaptive InSAR stack multilooking exploiting amplitude statistics: A comparison between different techniques and practical results," *IEEE Geosci. Remote Sens. Lett.*, vol. 8, no. 3, pp. 441–445, May 2011, doi: 10.1109/LGRS.2010.2083631.

[31] M. Jiang, X. Ding, Z. Li, C. Wang, W. Zhu, and L. Ke, "InSAR coherence magnitude estimation based on data stack," *Chin. J. Geophys.*, vol. 56, no. 3, pp. 799–811, Mar. 2013.

[32] M. Jiang, X. Ding, R. F. Hanssen, R. Malhotra, and L. Chang, "Fast statistically homogeneous pixel selection for covariance matrix estimation for multitemporal InSAR," *IEEE Trans. Geosci. Remote Sens.*, vol. 53, no. 3, pp. 1213–1224, Mar. 2015, doi: 10.1109/TGRS.2014.2336237.

[33] M. Jiang, X. Ding, X. He, Z. Li, and G. Shi, "FaSHPS-InSAR technique for distributed scatterers: A case study over the lost hills oil field, California," *Chin. J. Geophys.*, vol. 59, no. 10, pp. 3592–3603, Oct. 2016.

[34] M. Jiang, X. Ding, and Z. Li, "Homogeneous pixel selection algorithm for multitemporal InSAR," *Chin. J. Geophys.*, vol. 61, no. 12, pp. 4767–4776, Dec. 2018.

[35] M. Jiang and A. M. Guarnieri, "Distributed scatterer interferometry with the refinement of spatiotemporal coherence," *IEEE Trans. Geosci. Remote Sens.*, vol. 58, no. 6, pp. 3977–3987, Jun. 2020, doi: 10.1109/TGRS.2019.2960007.

[36] N. Cao, H. Lee, and H. C. Jung, "Mathematical framework for phase-triangulation algorithms in distributed-scatterer interferometry," *IEEE Geosci. Remote Sens. Lett.*, vol. 12, no. 9, pp. 1838–1842, Sep. 2015, doi: 10.1109/LGRS.2015.2430752.

[37] G. Fornaro, S. Verde, D. Reale, and A. Pauciullo, "CAESAR: An approach based on covariance matrix decomposition to improve multibaseline-multitemporal interferometric SAR processing," *IEEE Trans. Geosci. Remote Sens.*, vol. 53, no. 4, pp. 2050–2065, Apr. 2015, doi: 10.1109/TGRS.2014.2352853.

[38] S. Verde, D. Reale, A. Pauciullo, and G. Fornaro, "Improved small baseline processing by means of CAESAR eigen-interferograms decomposition," *ISPRS J. Photogramm. Remote Sens.*, vol. 139, pp. 1–13, May 2018, doi: 10.1016/j.isprsjprs.2018.02.019.

[39] C. Yu, Z. Li, and N. T. Penna, "Interferometric synthetic aperture radar atmospheric correction using a GPS-based iterative tropospheric decomposition model," *Remote Sens. Environ.*, vol. 204, pp. 109–121, Jan. 2018, doi: 10.1016/j.rse.2017.10.038.

[40] A. Pepe and R. Lanari, "On the extension of the minimum cost flow algorithm for phase unwrapping of multitemporal differential SAR interferograms," *IEEE Trans. Geosci. Remote Sens.*, vol. 44, no. 9, pp. 2374–2383, Sep. 2006, doi: 10.1109/TGRS.2006.873207.

[41] T. Li, H. Zhang, H. Fan, C. Zheng, and J. Liu, "Position inversion of goafs in deep coal seams based on DS-InSAR data and the probability integral methods," *Remote Sens.*, vol. 13, no. 15, p. 2898, Jul. 2021, doi: 10.3390/rs13152898.

[42] Q. He, Y. Zhang, H. Wu, and Y. Luo, "Mining subsidence monitoring with modified time-series SAR interferometry method based on the multi-level processing strategy," *IEEE Access*, vol. 9, pp. 106039–106048, 2021, doi: 10.1109/ACCESS.2021.3099633.

[43] B. Hu, J. Zhou, J. Wang, Z. Chen, D. Wang, and S. Xu, "Risk assessment of land subsidence at Tianjin coastal area in China," *Environ. Earth Sci.*, vol. 59, no. 2, pp. 269–276, Mar. 2009, doi: 10.1007/s12665-009-0024-6.

[44] H.-M. Wang, Y. Wang, X. Jiao, and G.-R. Qian, "Risk management of land subsidence in Shanghai," *Desalination Water Treatment*, vol. 52, nos. 4–6, pp. 1122–1129, Jan. 2014, doi: 10.1080/19443994.2013.826337.

[45] J. Guan, M. Gao, and H. Gong, "Discussion on the causes of regional differential settlement of Beijing-capital international airport," *Sci. Surv. Mapp.*, vol. 46, no. 9, pp. 67–75, Sep. 2021.

[46] B. Qi, Z. Pan, C. Feng, C. Tan, P. Zhang, J. Meng, M. Sun, X. Yang, X. Lei, H. Shi, and B. Yi, "Application of comprehensive geophysical-drilling exploration to detect the buried Shunyi active fault belt in Beijing," *Acta Geol. Sinica*, vol. 94, no. 4, pp. 1315–1329, Apr. 2020.

[47] P. Zhang, "Study on the Shunyi buried active fault and its induced ground fissure disaster in Beijing," Ph.D. dissertation, Chin. Acad. Geol. Sci., Beijing, China, 2021.
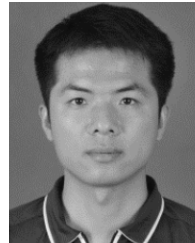
HUIFU ZHUANG (Member, IEEE) received the B.S. degree in geomatics engineering and the Ph.D. degree in geodesy and survey engineering from the China University of Mining and Technology, Xuzhou. He has been a Postdoctoral Researcher with the China University of Mining and Technology. His research interests include the area of remote-sensing image processing and information extraction, which include change detection, computer vision, image filtering, and matching.

QIAN HE received the M.S. degree in geodesy and survey engineering from the China University of Mining and Technology, Xuzhou. She is currently pursuing the Ph.D. degree in photogrammetry and remote sensing. Her current research interests include InSAR technology and application, remote sensing image processing, and land subsidence monitoring.

RUI WANG received the M.S. degree in cartography and geography information system from the Jiangxi University of Science and Technology (JXUST), Ganzhou. He is currently pursuing the Ph.D. degree with the China University of Mining and Technology. He is also teaching with JXUST. His current research interests include the quantitative remote sensing and ecological environment remote sensing.

XIN HE received the B.S. degree in information engineering from Hubei Normal University, Huangshi. She is currently working with Hubei YJT Technology Company Ltd., China. Her research interests include PCB design for precision instrument and remote sensing application.

JIAWEI CHEN received the B.S. degree in cartography and geography information system from the Jiangxi University of Science and Technology, Ganzhou. He is currently working with Ganzhou Liangye Technology Company Ltd., China. His current research interests include the natural disaster risk survey and disaster monitoring.

• • •